CHAPTER 6
XAFS CHARACTERIZATION OF EMBEDDED BIMETALLIC NANOCLUSTERS IN MULTILAYER FILM

6.1. Background

Bimetallic magnetic NCs embedded in non-magnetic matrix have gained impetus due to their ability wide-ranged applications. The employment of a matrix gives an additional degree of freedom and allows tuning the properties depending on the particle arrangement within the matrix. Additionally, the matrix stabilizes the NCs (even those present in non-equilibrium state), protects them from the environment, arrests their position and prevents coalescence. They are widely employed in (i) opto-electronic devices (for their large third-order susceptibility with pico second response time)[131] ((ii) surface lubricants for MEMS switch contacts; (iii) ultra high density data storage.[132-133] (iv) Catalysis[134-136], including specific reactions like hydrogenation of olefins and structural rearrangement (of Carbon skeleton) in hydrocarbons[137], decontamination of ground water[138], *Metal-filled carbon nanotubes* as electrocatalysts in fuel cells.[139]

Wetting being an issue in electronic devices, a dry method of synthesis would be advantageous. Several dry synthesis methods viz. lithography[140], co-sputtering[141], ion implantation[142], laser ablation[143] have also been used previously for embedded NC synthesis. Over the years, Ion irradiation has gained importance as a method for synthesis/modification/characterization materials depending on the energy of the incident ions (~keV to GeV).[144] Ion irradiation results in a variety of ion-solid interactions, including (i) incorporation of ions into the solid, (ii) creation of vacancies (defects and interstitials), (iii) sputtering (ejection of atoms and molecules), depending on the energy

of the incident ion. Energetic ions, during their passage through a material lose energy via two processes: Nuclear energy loss S_n and electronic energy loss S_e. S_n refers to energy loss due to elastic collisions of the incident ions with the atoms in the material, and is dominant at low energies (~ keV to 1 MeV). It results in atomic displacement from their lattice sites either by ejection from the surface or by relocation within the solid. S_e refers to the energy lost by inelastic collisions of the ion with the atoms in the material, leading to ionization or excitation of the atoms. It is dominant at high energies (>>1MeV).

In multilayer (ML) thin films, MeV ion irradiation has been observed to introduce a number of effects with interesting consequences. In magnetic *Co/Pt* MLs, interfacial mixing induced by ion irradiation resulted in spin-reorientation transition, and change of giant magnetoresistance.[145] Small concentrations of magnetic impurity in non magnetic layers of a magnetic ML, which can cause changes in magnetic coupling and magnetoresistance[146], can be introduced in the non-magnetic layers by ion irradiation. In general, irradiation induced inter-layer mixing, interfacial broadening and period dilation is commonly observed in MLs[147-148], as demonstrated in several previous reports.[149- 152]

A *Pt/C* ML has been used as a regular X-ray mirror.[153-154] Addition of a *Ni* layer is expected to extend the functional energy range beyond 80 keV, i.e. beyond the *Pt* K-edge. Ion irradiation of the mirror was intended to simulate the defects that could possibly be induced by high-flux, high-energy X-rays, in order to understand device functionality.

However, the main impact of this work lies beyond mirror assessment in terms of damage. Instead, we explore the possibility/feasibility to synthesize bimetallic (magnetic) *Ni/Pt* clusters on (non-magnetic) *C* matrix by ion irradiation of *Pt/Ni/C* multilayer (ML). *C* is selected for its low density (2.5g/cc) and high stiffness (> glass). Additionally, Carbon can provide magnetic isolation between neighboring clusters, which causes the reduction of inter-particle exchange coupling.

This method would be unique in the sense that, if successful, it would lead to the generation of ML structure which contains alternating layers of magnetic clusters embedded in non-magnetic matrix separated by magnetic layers.

Herein, the control parameter for composition of the bimetallic clusters will not be limited to thermodynamics alone, but can be controlled by collision kinetics, initial thickness of the layers and interfacial integrity.

6.2 Sample Synthesis details

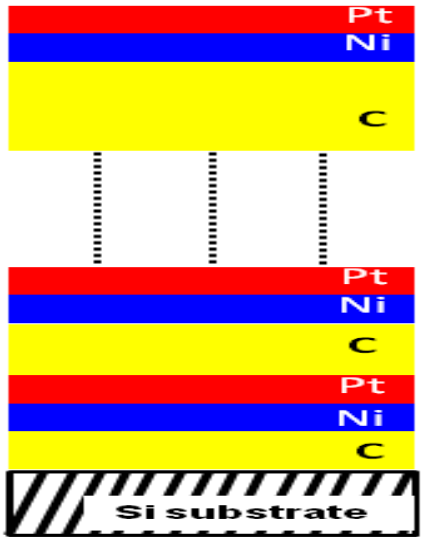

Fig. 6.1: Schematic of the deposited multilayer

A depth graded *Pt/Ni/C* multi tri-layer (15 tri-layers in the multilayer stack), in which the thickness of the *C* layer gradually varies with depth, was prepared by alternate deposition of *Pt*, *Ni* and *C* layers on a 30mm×70mm float glass substrate by ion beam sputtering technique [155,167] at a low Argon pressure of 0.1 mbar. Tri-layer periodicity, d ~ 7 nm. Schematic of the multilayer is shown in Fig. 6.1. 20mm ×4mm pieces of the sample were cut and irradiated with 2 MeV Au^{2+} ions 2×10^{15} ions/cm^2 at the 3MV Pelletron accelerator at the Institute of Physics, Bhubhaneshwar (India).

6.3 Structural characterization of the ML pre-and post-irradiation

Several techniques can be used to probe ion-irradiation induced changes in MLs. Transmission Electron Microscopy (TEM) and Scanning Electron Microscopy (SEM) can be used to gain insight into the multilayer structure. X-ray Reflectivity (XRR) and Neutron Reflectometry can be used to determine roughness and thickness of individual layers. X-ray Fluorescence (XRF) is generally used to detect inter-layer mixing, X-ray Photoelectron Spectroscopy (XPS) can be used to chemically characterize the surface of the ML.

In this work, micro-structural details of the ML were derived using X-ray Reflectivity (XRR), X-ray Fluorescence (XRF) and Transmission Electron Microscopy (TEM).[157]

TEM measurements on the samples[157] revealed well separated Pt, Ni and C layers in the pre-irradiated (pristine) ML (Fig. 6.2). The irradiated ML shows mixing between the layers and some dark spots in the C layers[157], which could be nanoscale particles of higher density material within the C layers. Negative heat of mixing between Ni and Pt favors formation of Ni-Pt alloy. In contrast, positive heat of mixing between Ni and C and Pt and C favors segregation. Therefore, the observed clusters are likely to contain Ni and Pt. The average diameter of the clusters was determined to be ~ 1.7 nm, with size dispersion of ~10 %. The average inter-cluster separation was determined to be ~ 3.6 (0.9) nm and 0.8 (0.1) nm across the plane of C layer.[157]

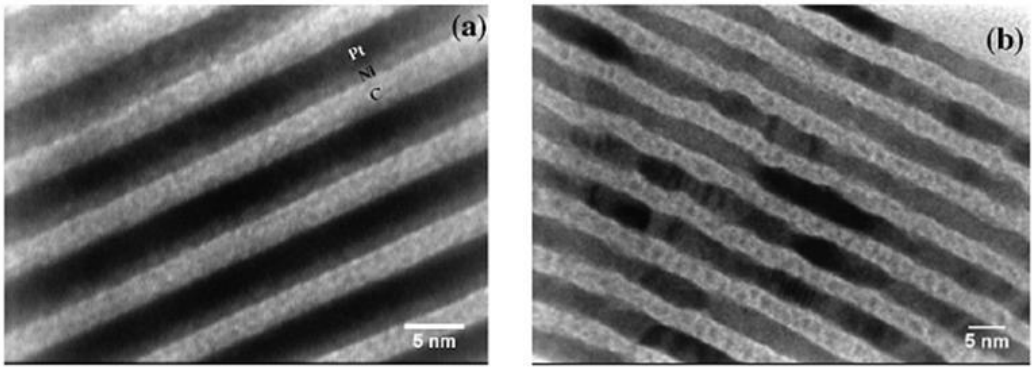

Fig. 6.2: XTEM micrographs of (a) pristine and (b) irradiated (ion fluence = 2×10^{15} ions/cm^2) samples. [157]

XRR and XRF were recorded in X-ray Standing Wave mode to overcome the limitations of conventional XRR and XRF.

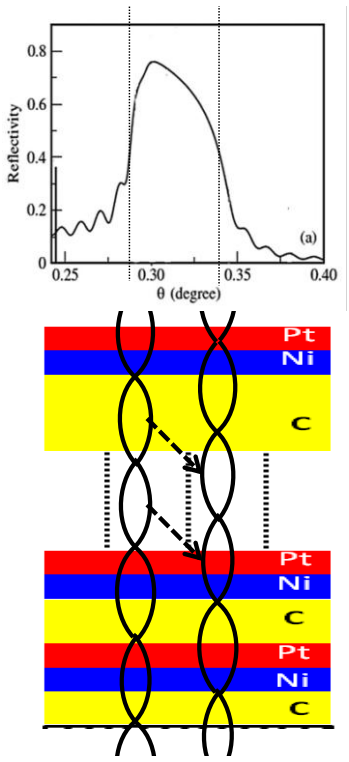

Fig. 6.3: Illustration of formation of standing waves of X-rays in Pt/Ni/C Multilayer. As the angle of incidence increases through the diffraction peak region (top), antinodes move from the low electron-density medium (C layers) to the high electron-density medium (Pt layers) (bottom).

The XSW technique is extensively used in condensed matter science. In a periodic ML, XSW are generated when Bragg diffraction occurs from the

ML.[156] The standing wave pattern has the periodicity of the corresponding diffraction planes (typically 0.2 nm). In this case atomic displacements of typically one-hundredth of this distance (i.e. 2 pm) can be detected, along with details of the displacement direction (inward or outward). Details of XSW technique are given in the next section. Fig. 6.3 schematically shows the formation of standing wave patterns while a first order Bragg diffraction of x-rays occurs from a periodic ML. At the rising edge of the Bragg peak, the antinodes of the standing wave are in the C layers. As the grazing angle of incidence advances through the Bragg peak, the standing wave pattern moves inward finally moving by half the ML period (*d*) at the falling edge of the Bragg peak, where the antinodes coincide with the Pt layers. The intensity of emission of fluorescence is proportional to the intensity of x rays.

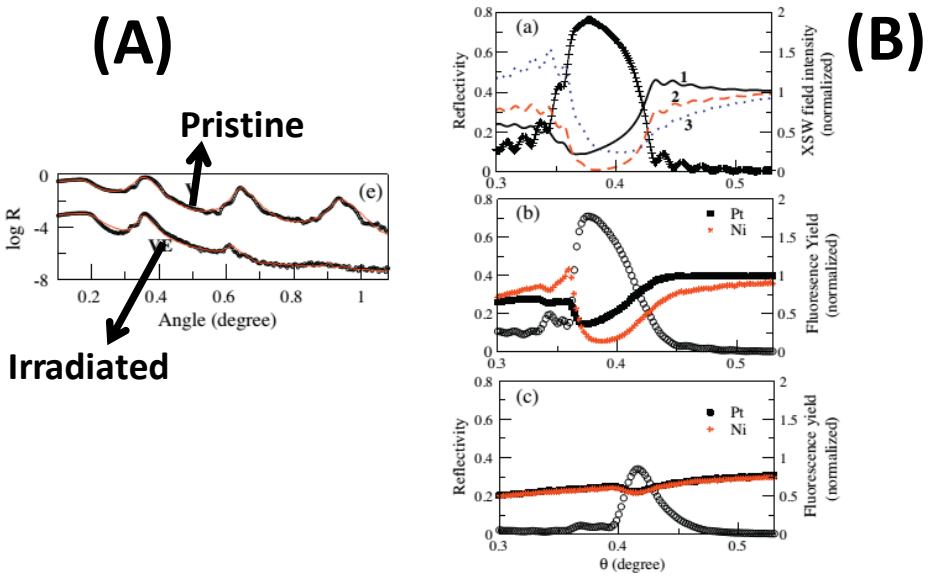

Fig. 6.4: (A) X-ray Reflectivity of pristine and irradiated MLs. (B) (a) Reflectivity under first order Bragg peak and integrated field intensities in 1-Pt layer, 2-Ni layer and 3-C layer. Reflectivity data and fluorescence yield for (b) pristine and (c) irradiated samples.[157]

Fig. 6.4 (A) shows the reflectivity plot for the pristine and irradiated samples.[157] Clearly there is an increase in interlayer roughness with irradiation. Fig. 6.4 (B) shows the

fluorescence yields for both the samples. Clearly the Pt- and Ni-fluorescence yields are almost indistinguishable in the irradiated ML (Fig. 6.4 (B) (c)). This indistinguishability implies that the Pt and Ni layers are completely mixed at this ion-fluence.

The knowledge from these structural studies had limitations of cluster details and the origin of assumed cluster configuration. In this context, XAFS would provide first-hand impression[150,157] of the cluster structure, for the given irradiation condition. For example, our results would establish if *Ni* and *Pt* form isolated clusters in *C*-matrix or core-shell structure[158-159] or alloy. These predictions cannot be drawn simplistically from bulk binary phase diagrams since factors such as surface energetics[160], *Ni/C* or *Pt/C* interactions (*i.e.* ternary phase diagrams), could come into play.

XAFS at *Ni K*-edge can (in principle) detect possible *Ni-Pt* alloy formation[161-162] at the *Ni-Pt* interface or *Ni-C* compound formation[163-164] at the *Ni-C* interface. These changes are typically reflected in coordination or bond-lengths in EXAFS results or *whiteline* features (oxidation state) in XANES.

To solve this problem, it is clear that XAFS cannot be measured in normal reflection mode, since it would be impossible to separate information coming from the layers and the interfaces, which is the key to decoding the structure of the ion irradiation generated clusters. The layers and interfaces of the ML can be selectively filtered for information by x-ray standing wave (XSW) technique. The standing-wave field is generated within the periodic ML as a result of a superposition of incident and diffracted waves when x-rays are Bragg reflected by the periodic ML.[165-166] The equi-intensity planes of the standing-wave field are parallel to and have the periodicity of the diffracting planes in the periodic MLs. At an angle of incidence corresponding to the rising edge of the diffraction peak, the antinodal planes of the standing-wave field lie between the diffracting planes. As the angle of incidence increases, the antinodal planes move

continuously inward onto the diffracting planes at the falling edge of the diffraction peak. Over the angular region of Bragg reflection, emission of fluorescent X-rays[165-166] from the periodic ML is strongly modulated, being at a maximum (minimum) when the antinodal (nodal) planes coincide with positions of the atoms in the periodic ML. Bragg diffraction is also obtained from a ML with a slightly varying period and consequently XSW is generated in such graded MLs. By scanning across the Bragg angle, we center the antinode successively in each layer. The present system is same as described in Ref. 157 and 167. On the Bragg peak [Fig. 6.5(a)], we select two angles on rising ($\theta = 0.554^{o}$) and falling ($\theta = 0.638^{o}$) edges of the Bragg peak which we refer to as "low" and "high" respectively. For the present pristine ML system, although the low angle corresponds to the location of antinodes on the *C* layer, rising edges of the antinodes coincide with the *Ni/C* interfaces [Black curve: Fig. 6.5(b)]. Fluorescence-mode *Ni K*-edge XAFS for this angle, therefore, yields the structural information around *Ni* diffused into *C* layer. At the high angle, the anti-nodes coincide with *C/Pt* interfaces [blue curve: Fig. 6.5(b)]. However, the main contribution to *Ni* fluorescence comes from the relatively denser *Ni* atomic concentration at *Pt/Ni* interfaces as the falling edges of the antinodes coincide with these interfaces [Fig.6.5 (b)]. Therefore, *Ni K*-edge XAFS at high angle reveals the *Ni* environment predominantly at the *Pt/Ni* interface[iii]. Any dissolved *Ni*, although expected to be in very small amount at this interface, can contribute to the observed *Ni* fluorescence. In the irradiated ML, the XSW-pattern shifts due to changes in structure (mixing) and density. At low angle, the antinodes of XSW coincide with the *C* layer of the irradiated ML while the nodes coincide with the *Ni/Pt* interface [or rather, at the

[iii] In the system under consideration, the thicknesses of the *Pt* layer and *Ni* layer are 23 Å and 22 Å respectively. The thickness of the *C* layer was varied from 29.7 Å (at the bottom-most layer) to 35.7 Å (at the top-most layer), since the system is a depth graded multilayer. Despite the location of anti-node at interfaces, there will be some contribution to the signal from the non-interfacial regions of the layers.

middle of the mixed *Ni-Pt* layer as in Ref. 157] (Black curve, Fig.6.5 (b)). *Ni K* edge XAFS at this angle, for the irradiated ML, reveals structural information around *Ni* diffused into *C* layer (as in the pristine ML). At high angle, the antinodes of the XSW shift to the *Ni/Pt* interface or the middle of the *Ni-Pt* layer (instead of *C/Pt* interface as in pristine ML) while the nodes are located in the *C* layer [Blue curve, Fig. 6.5 (b)]. Therefore, *Ni K* edge XAFS at this angle reveals the structural information around *Ni* at *Ni/Pt* interface of irradiated ML.

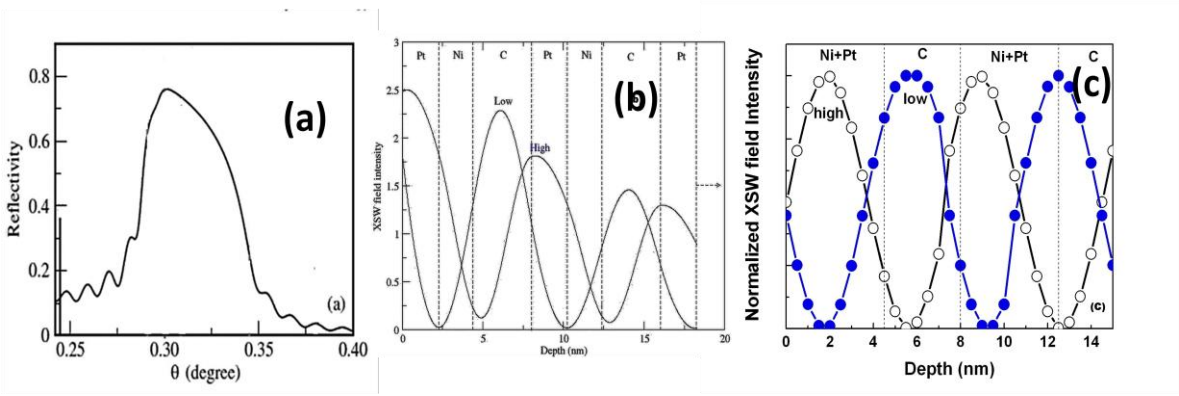

Fig. 6.5: (a) First order Bragg peak; the positions of antinodes and nodes of the X-ray standing wave (XSW) formed within the first few layers (7 consecutive layers from surface) of our graded *Pt/Ni/C* multi-trilayer in (b) Pristine ML and (c) Irradiated ML. The black curve corresponds to the angle chosen in left (lower angle) side of the Bragg peak (BP) while the blue curve corresponds to the angle chosen at the right (high angle) side of the BP.

The structural model is retrieved mainly from the XAFS coordination results. We theoretically calculated the coordination number for various degrees of interfacial mixing and compared with the XAFS results. The theoretical coordination calculation is non-trivial, having to include the variation in field intensity over the individual layers of the ML from XSW pattern (since this causes variation in the number of *Ni* atoms excited in

different depths over a period of the ML sample).[iv] With rigorous XAFS analysis, we are able to derive finer (beyond XRR/XRF/XTEM) micro-structural details: e.g. quantification of intermixing, chemical nature of mixing, cluster identification. The most important outcome is the identification of bimetallic nano-clusters formed within irradiated *C* matrix.

6.4. XAFS Experimental details

XAFS data were collected in fluorescence mode at the *Ni-K* edge (8.333 keV) at the ROEMO (E2) beamline at Hamburg Synchrotron Radiation Laboratory (HASYLAB) at DESY, Germany. A pair of Si *(111)* crystals in parallel geometry was used as monochromator to filter out the wavelengths. The first *Si (111)* crystal in the path of the incident beam was given suitable offset (from parallel geometry) to suppress higher harmonics from the monochromator. During energy scan of EXAFS experiments, an appropriate adjustment of the angle of incidence was made in order to maintain the antinodal positions within the sample unchanged. A *Si (Li)* detector was used to collect the fluorescence photons.

6.5. Results and discussion

6.5.1 XAFS results

The XAFS data sets (Fig. 6.6a) were analyzed for the first coordination shell around *Ni*. The rather large noise (possibly due to disordered interface) in the data precluded higher shell analysis. However, the first shell (nearest neighbor) analysis is

[iv] The penetration depth of 2 MeV Au^{2+} ions being ~microns ions go through the ML sample and get embedded deep into the substrate; the variation due to ion impact factor is negligible.

found to sufficiently extract the irradiation-induced structural changes (shown below). Correlation-free coordination (N) and Debye Waller Factor (DWF) were obtained by simultaneously fitting each dataset for k^w (w = 1, 2).[v] The data were fit over the k-range 2.2-8 Å^{-1} and r-range 1.2-3.4 Å. The results are listed in Table 6.2. An example of fit quality (R-factor = 0.001-0.014) is shown in Fig. 6.6b.

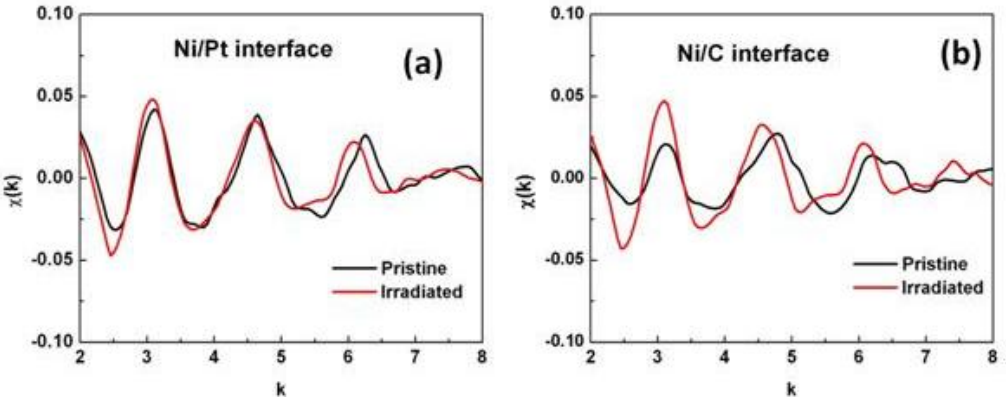

Fig. 6.6a: Comparison of data in k-space before and after irradiation for (a) Ni/C interface and (b) Ni/Pt interface

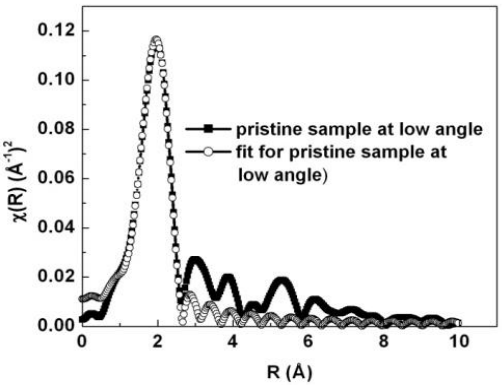

Fig. 6.6b: Comparison of data with fit

Several fitting strategies were considered to test the robustness of the fit parameters, such as (or non-) inclusion of third cumulant[vi] into disorder, (or non-) constraining the coordination number around *Ni* to 12 (fcc) or that between the pristine

[v] Simultaneous fitting of the datasets was necessary in order to have sufficient variables for fitting.

[vi] The third cumulant is a measure of the anharmonicity in the atomic distribution.

and irradiated MLs to be the same. The error bars in Table 6.1 reflect the maximum possible variation from all these fits.

6.5.1.1 Low angle (*C* layer and its interfaces with *Ni* and *Pt*)

XAFS data for *pristine* ML at low angle was fit by considering *Ni-Ni* and *Ni-C* scattering paths (any attempt to include *Ni-Pt* path resulted in a bad fit; this is not surprising as there are nodes in the XSW pattern at the *Pt/Ni* interfaces). The large error bars for N_{Ni-C} are due to the extremely low *Ni-C* coordination.

TABLE 6.1. XAFS fit results for Pt/Ni/C ML

Bond	ML	N	σ^2 (Å^2)	R(Å)	Theoretical R(Å)
		Low Angle			
Ni-Ni	Pristine	5.46 ± 0.12	0.018 ± 0.0004	2.445 ± 0.003	2.48
	Irradiated	6.24 ± 0.17	0.021 ± 0.0005	2.612 ± 0.001	
Ni-C	Pristine	0.88 ± 0.18	0.016 ± 0.006	1.964 ± 0.007	2.00
	Irradiated	0.33 ± 0.18	0.016 ± 0.006	1.964 ± 0.007	
Ni-Pt	Pristine	-	-	-	2.60
	Irradiated	4.14 ± 0.14	0.024 ± 0.002	2.727 ± 0.007	
		High Angle			
Ni-Ni	Pristine	7.27 ± 1.11	0.021 ± 0.003	2.54 ± 0.01	2.48
	Irradiated	8.49 ± 0.92	0.025 ± 0.003	2.60 ± 0.01	
Ni-Pt	Pristine	3.4 ± .	0.016 ± 0.009	2.72 ± 0.04	2.60
	Irradiated	3.51 ± 0.92	0.02 ± 0.01	2.76 ± 0.03	

From Fig. 6.6(b), it is clear that in the data there are contributions from part of the *Ni* layer, *Ni/C* interface and (possible) diffused *Ni* atoms in the bulk *C* layer. Considering interfacial planes to be {111}/{100}/{110} and taking into account the relative variation

in field intensity across the ML (as explained earlier) (Refer Fig. 6.6(b)), the weighted-average *Ni-Ni* coordination may be formulated as[vii-ix168-170]:

$$N_{Ni-Ni} = \frac{[(12 \times \frac{\int I_{Ni}}{\int I_0} \times N_A) + (8.33 \times \frac{\int I_{Ni/C}}{\int I_0} \times N_B)]}{(\frac{\int I_{Ni}}{\int I_0} \times N_A) + (\frac{\int I_{Ni/C}}{\int I_0} \times N_B)} \quad (6.1),$$

where N_A is the number of *Ni* atoms in *Ni* layer, N_B is the number of interfacial *Ni* atoms, I_{Ni} is the intensity in *Ni* layer, I_C is the intensity in *C* layer, $I_{Ni/C}$ is the intensity at *Ni/C* interface, I_0 is the maximum intensity, in this case, I_C.

The first and second terms in the numerator reflect the contribution from *Ni-Ni* bonds in *Ni* layer and at *Ni/C* interface respectively. (Note that *Ni* cluster formation inside *C* layer is excluded preliminarily). The denominator represents the sum of *Ni* atoms excited in *Ni* layer and *Ni/C* interface. Assuming the interfacial roughness ($\sigma_{Ni\text{-}C}$ = 1.7 Å, from reflectivity experiments) to be preliminarily representative of interfacial extent and the thickness of *Ni* layer = 22 Å, interface-volume ratio $\frac{N_B}{(N_A + N_B)} = 7\%$. However, this ratio should have yielded $N_{Ni-Ni} = 11.63$ from Eq. (6.1) (instead of 5.4 in Table 6.1).

On the other hand, the average interfacial *Ni-C* coordination (for adsorption) may be formulated as:

$$(N_{Ni-C})_{\max} = \frac{3.67 \times \frac{\int I_{Ni/C}}{\int I_0} \times N_B}{(\frac{\int I_{Ni}}{\int I_0} \times N_A) + (\frac{\int I_{Ni/C}}{\int I_0} \times N_B)} \quad (6.2).$$

[vii] Bulk Ni fcc lattice has 12 neighbors while interfacial Ni has 9 neighbors. 3 missing neighbors correspond to dangling bonds for {111} plane. In the case of {110} and {100} planes, interfacial Ni has 8 neighbors and the 4 missing neighbors correspond to dangling bonds. Since the layers are polycrystalline in the sample, we have to consider an average over these three planes.

[viii] The intensity variation (Figure.1) in the various layers is normalized with respect to the intensity in the (i) C layer for low angle of the Bragg peak and (ii) Pt layer for high angle of the Bragg peak.

[ix] There are no *Ni* atoms at the *C/Pt* interface.

Table 6.2: XAFS coordination analysis steps for Ni/C interface*

1. Using XRR determined roughness layer thickness, calculate fraction of Ni atoms at Ni/C interface
2. From the normalized XSW intensity variation across the ML, extract the no. of x-ray excited *Ni* atoms ((N_{Ni}) ex) (that contribute to XAFS signal), at different locations of the ML.
3. Considering the structure of *Ni* -layer to be *fcc* and the *Ni/C* interfacial plane to be consisting of {111}:{110}:{100} =1:1:1, calculate the weight-averaged surface coordination for *Ni* atoms at this interface.
4. Using equations 6.1 and 6.2, calculate the weighted average $N_{Ni\text{-}Ni}$ and $(N_{Ni\text{-}C})_{max.}$
5. If $(N_{Ni\text{-}Ni})_{calculated} \neq (N_{Ni\text{-}Ni})_{XAFS}$ and $(N_{Ni\text{-}C})_{max.} < (N_{Ni\text{-}C})_{XAFS}$, the interface is not sharp and some Ni atoms are pre-diffused into C layer.
   $(N_{Ni\text{-}C})_{C\ layer} = (N_{Ni\text{-}C})_{XAFS} - (N_{NiC})_{interfacial}$
6. Calculate % of Ni atoms diffused into C layer

*The above procedure is true for all interfaces

From this equation, $N_{Ni\text{-}C}$ = 0.37 (instead of 0.879 in Table 6.2). Lower $N_{Ni\text{-}Ni}$ (in Table 6.1) and higher $N_{Ni\text{-}C}$ (compared to calculated results from above eqn.) suggest replacement of some *Ni* near neighbors by *C* atoms, possibly due to additional (random) diffusion of *Ni* into *C* layer (beyond the reflectivity-derived simplistic binary model of layer + interface) (Fig.. 6.7). Solving Eq. (6.2) for XAFS-derived coordination yielded this additional *Ni* proportion to be 26%.[x] Thus, the salient conclusion on the pristine *Ni/C* interfacial structure, from XAFS (and beyond XRR), is the existence of significant proportion of sporadic pre-diffused *Ni* atoms within *C* layer. The implications of this finding will be evident later in this paper.

The nature of *Ni-C* bond is determined to be chemical from XANES: XANES at *Ni K*-edge (Fig. 6.8(a)), for the pristine ML, shows conspicuous (positive) deviation of *Ni*

[x] Total $N_{Ni\text{-}C}$=0.88, out of which 0.37 is interfacial. This implies that 0.51 is in C layer. Now, each Ni atom in C layer has 2 C coordination (amorphous carbon). 2×(total no. of Ni atoms) contribute to $N_{Ni\text{-}C}$ =0.51 Therefore % of Ni atoms diffused into C layer = 0.51/2 = 26%.

valence from that of pure *Ni* (i.e. 0 oxidation state). We attribute the integrity of *Ni/C* interface, during irradiation, to this chemical binding.

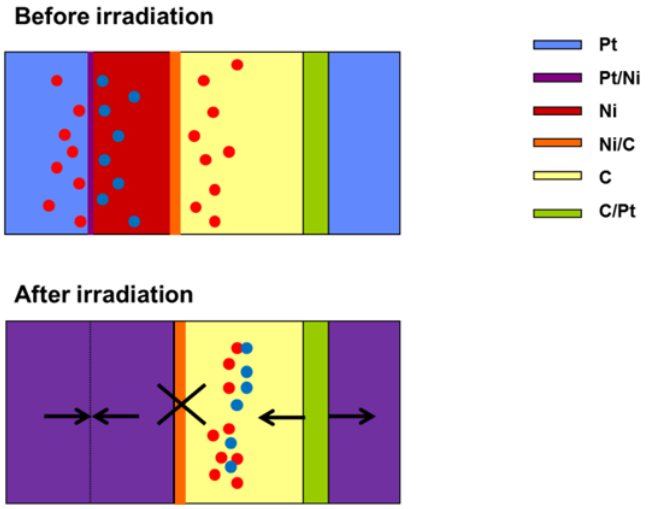

Fig. 6.7: Structural model for the multilayer before and after irradiation.

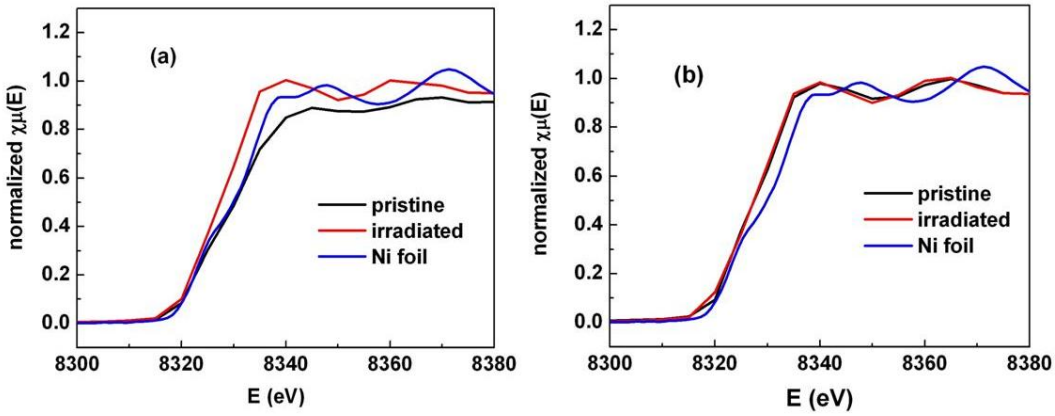

Fig.6.8: XANES at (a) *Ni/C* interface and (b) *Ni/Pt* interface

The data for the *irradiated* ML was best fit by *Ni-C*, *Ni-Ni* and *Ni-Pt* scattering paths (simulations for different values of $N_{Ni\text{-}Ni}$ (and $N_{Ni\text{-}Pt}$) reveal resolution limit of $\Delta N = 2$). The emergence of *Ni-Pt* coordination (in contrast to pristine ML) is consistent with XTEM results and due to irradiation-induced diffusion of *Pt* atoms into C layer (suggested by XRR). [*Pt/C* interfaces[171,172] are reported to be vulnerable due to absence of *Pt-C* chemical bond[173], unlike *Ni-C*.[174] This is consistent with increase in roughness with irradiation in Ref. 157: $\sigma_{Pt/C}$ increases by ~ 400% while the corresponding increase in

$\sigma_{Ni/C}$ is by 32%]. The bond-length changes are consistent with the mixing of *Ni* and *Pt*. *Ni-Ni* bond-length (2.44 Å), which is close to the metallic value (2.48 Å) before irradiation, expands (to 2.6 Å) towards *Pt-Pt* bond-length (2.7 Å) after irradiation. This bond-length change is duly directed towards accommodating the larger intercalated *Pt* atoms.

6.5.1.2 Cluster Models

While XTEM indicates the formation of *Pt-Ni* nanoclusters, it is unable to determine their exact configuration. We consider various models of nano-clusters to deduce the configuration of *Ni-Pt* within *C* layer (i) isolated clusters of *Ni* and *Pt*; (ii) *Ni* core - *Pt* shell; (iii) *Pt* core – *Ni* shell; (iv) *Ni*-centered icosahedral bimetallic cluster [Icosahedral model has been considered since this is a highly disordered system. In highly disordered systems (for e.g. metallic glass), such icosahedral structural units have been observed[175]] and (v) *Pt*-centered icosahedral bimetallic cluster. (Fig. 6.9)

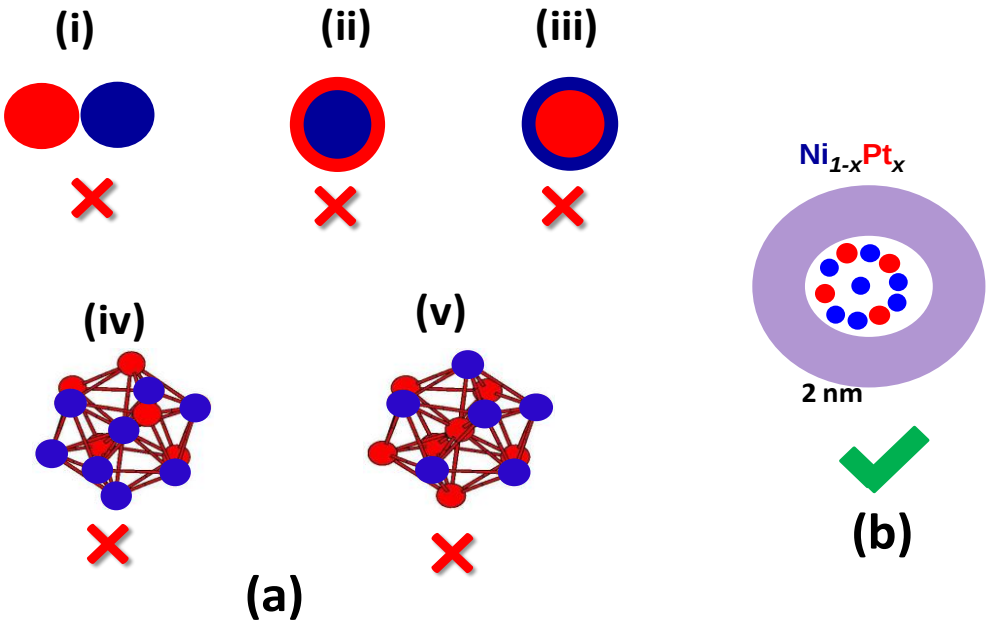

Fig. 6.9: (a) Various cluster models considered, (b) final model for embedded clusters in C layers

For this, the contributions to $N_{Ni\text{-}Ni}$ from *Ni/C* interface, *Ni+Pt* mixed layer and within *C* layer were decoupled.[xi] Subtracting the interfacial contribution and *Ni+Pt* layer contribution from the total in Table 6.2, $N_{Ni\text{-}Ni}$ (from *C* layer) and $N_{Ni\text{-}Pt}$ are calculated to be 6.35 and 3.64 respectively. Next, for models (i-iv) we calculated $N_{Ni\text{-}Ni}$ and $N_{Ni\text{-}Pt}$ for different surface-volume ratios of the number of *Ni* atoms[xii] (*i.e.* different cluster sizes of *Ni*).

Model (i) is ruled out since experimentally-deduced $N_{Ni\text{-}Ni}$ (~6.35) is significantly lower than that for the smallest *Ni* cluster. On the other hand, significant $N_{Ni\text{-}Pt}$ (~ 3.64) rules out isolated *Pt* clusters. The same logistics rule out Model (ii), since the latter would have resulted in a minimum $N_{Ni\text{-}Ni}$ ~ 9. Model (iii) is ruled out since our $N_{Ni\text{-}Pt} > 0.3$.[xiii] Model (iv-v) would have resulted in $N_{Ni\text{-}Ni} + N_{Ni\text{-}Pt} \sim 7$. The same being ~ 9 from our XAFS results rules out 13 atom icosahedral clusters.

Therefore, *Ni-Pt* bimetallic clusters around *Ni* centre, having *Ni:Pt* = 0.6:0.4, highly disordered beyond the first shell, may be the best representation for the *Ni/Pt* configuration within the *C* layer. The first shell radius of the clusters is estimated to be ~ 0.25 nm, corresponding to *Ni-Pt* bond-length in Table 6.1. The solution is consistent with *Ni-Pt* alloy formation, as indicated by *Ni-Pt* binary phase diagram for this atomic concentration ratio. Previous reports on *Ni/Pt* alloys have shown clusters of this particular composition to be ferromagnetic.[176-178]

[xi] The integrated intensities for each interface and layer were calculated. The total $N_{Ni\text{-}Ni}$ has contributions from *Ni+Pt* mixed layer + *C* layer + *Ni/C* interface.

$$[N_{Ni-Ni}]_{Total} = \frac{N_{Clayer} \times \int I_C + N_{Ni+Ptmixedlayer} \times \int I_{Ni+Pt} + N_{Ni/C} \times \int I_{Ni/C}}{\int I_C + \int I_{Ni+Pt} + \int I_{Ni/C}}$$

[xii]

$$N_{Ni-Ni} = 12(1-x) + 9x; N_{Ni-Pt} = 3x$$

[xiii] Pt core, Ni shell would imply that surface Pt atoms see an average of 3 Ni nearest neighbor, assuming the surface to be (111). So each Ni atom will see 1/3 = 0.3 Pt atoms.

6.5.1.3 High Angle (*Ni-Pt interface*)

The data for both the pristine and the irradiated MLs (Fig. 6.10) were best fit by *Ni-Ni* and *Ni-Pt* scattering paths. (Note that any attempt to include *Ni-C* path resulted in bad fit.). Metallic interfaces are generally marked by intermixing[179] between the layers: *Ni-Pt* form alloys[180-181]at very low energies. Lower $N_{Ni\text{-}Ni}$ (~ 7.3) and increased $N_{Ni\text{-}Pt}$ (~3.4), for the pristine ML, compared to those theoretically calculated [replacing I_C by I_{Pt} (Intensity in *Pt* layer) and $I_{Ni/C}$ by $I_{Ni/Pt}$ (Intensity at *Ni/Pt* interface) in Eqn.(6.1)-(6.2)] for ideal sharp interface[xiv] implies pre-existing intermixing, consistent with XRR. From the coordination ratio $N_{Ni\text{-}Ni}$:$N_{Ni\text{-}Pt}$ (and density), the atomic concentration ratio *Ni:Pt* was calculated to be 0.82: 0.16. *Ni-Pt* binary phase diagram suggests the possibility of alloy formation for this concentration ratio.[163] This is further supported by XANES at *Ni K*-edge (Fig.6.8(b)) for the pristine ML, which shows conspicuous (negative) deviation from that of pure *Ni* (i.e.0 oxidation state). It implies charge transfer to *Ni* at this interface, most likely from *Pt*.[182] Therefore, *Ni-Pt* alloy could be reasonably justified structural representation for this interface.

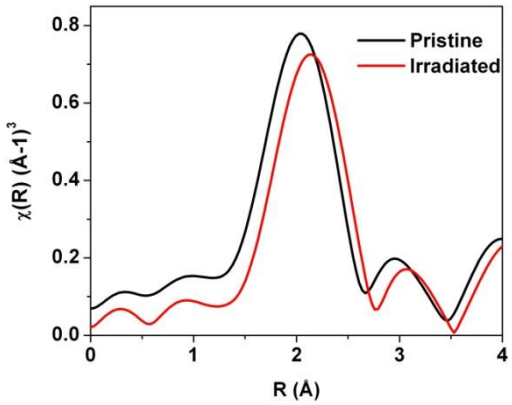

Fig. 6.10: Fourier Transform for both the MLs at *Ni/Pt* interface

For the irradiated ML, $N_{Ni\text{-}Ni}$ and $N_{Ni\text{-}Pt}$ were calculated for various degrees of interfacial mixing and by including the intensity variation. It is deduced that interlayer

[xiv] Ideal sharp interface implies that there is no diffusion between the layers beyond the interface.

diffusion of 54% *Pt* →*Ni* and 22% *Ni* → *Pt* best matches with the XAFS coordination.[xv] The asymmetry in diffusion is consistent with pre-existing vacancy in *Ni* layer (due to 26 % *Ni* →*C* diffusion), which accommodates the apparently extra *Pt* atoms.[xvi]

Comparing the results for pristine and irradiated *Ni/Pt* interfaces, we observe significant enhancement in interfacial broadening (consistent with XRR) due to ion-driven diffusion, depicted in Fig. 6.7. The oxidation state of *Ni* remains unchanged, as confirmed by the similarity in the XANES spectra (Fig. 6.8(b)) for both the pristine and irradiated MLs. Thus, XAFS conclusion of *Ni/Pt* interface (beyond XRR) is the quantification of degree of atomic mixing and alloy composition of the interface.

6.5.2 Cluster Formation Method

We now decouple the role of kinetics, thermodynamics and nature of interfaces in cluster formation. The nature of interface (i.e. chemically bound/physically bound) determines the relative ratio of metallic diffusion into *C* matrix. This in turn determines the composition/density of the bimetallic clusters.

In this case, *Pt/C* is a physically bound interface due to large positive heat of mixing between *Pt* and *C*; hence it is susceptible to ion irradiation.[171-173] On the other hand, *Ni/C* is chemically bound[174] (Ni-carbide compound formation) and hence less susceptible to ion irradiation. *Ni/Pt* is an alloyed interface. As a result, ion irradiation induces diffusion of large number of *Pt* atoms into *C* layer, while the number of *Ni* atoms diffusing from *Ni/C* interface is much lower. (Note that from our XAFS coordination results, *Ni/C* interface is unaffected by ion irradiation).

[xv] The following equations were used to deduce the degree of mixing between Ni and Pt layers:

$$N_{Ni-Ni} = \frac{[(12\times(N_A-\Delta N)\times\frac{\int I_{Ni}}{\int I_0}+(8.33\times\frac{\int I_{Ni/Pt}}{\int I_0})\times N_B}{(\frac{\int I_{Ni}}{\int I_0}\times N_A)+(\frac{\int I_{Ni/Pt}}{\int I_0}\times N_B)}, \quad N_{Ni-Pt} = \frac{(12\times\Delta N\times\frac{\int I_{Pt}}{\int I_0})+(\frac{1}{12}\times\Delta N\times\frac{\int I_{Ni}}{\int I_0})+(3.67\times\frac{\int I_{Ni/Pt}}{\int I_0}\times N_B)}{(\frac{\int I_{Pt}}{\int I_0}\times\Delta N)+(\frac{\int I_{Ni}}{\int I_0}\times N_A)+(\frac{\int I_{Ni/Pt}}{\int I_0}\times N_B)}$$

ΔN = no of *Ni* atoms exchanged, N_A = no. of Ni atoms in Ni layer, N_B = no. of Ni atoms at Ni/Pt interface.

[xvi] Note that total Ni vacancy, due to diffusion = 26 % (Ni→C) + 22% (Ni →Pt) = 48%, is consistent with total Pt → Ni diffusion = 54%

6.5.3 Significance of Cluster Results

A remarkable aspect of these clusters is the presence of large disorder beyond the nearest neighbor, similar to our observation for multi-component metallic glasses. Notably, ordering features persisted up to second nearest neighbor for our bimetallic glasses. The striking difference in the degree of disorder between multi-component and bimetallic glasses is understandably consistent with "confusion principle".[175] In contrast, we observe that the bimetallic clusters formed on *C* matrix (induced by ion irradiation) are far more disordered and resemble multi-component cluster characteristics. Carbon matrix possibly helps the amorphous structure.[183] Highly disordered clusters, resembling glassy structure, find usage as patterned magnetic recording media. Their amorphous nature promotes growth in preferred orientation.[184] Moreover, glasses being defect free, the issue of different bits having different switching fields due to defects can be avoided (during writing).[185] Thus, ion irradiated *Pt/Ni/C* ML offers promise as magnetic device.

The subsequent design goal in ion-irradiation based fabrication method should be optimization of the cluster composition (to tune T_c, susceptibility etc.[175]), size and inter-cluster separation (to tune luminescence properties) by selection of matrix and metals, controlling interfacial charge transfer, layer thickness, ion flux etc.

6.4. Conclusion

We have probed the structural changes of a *Pt/Ni/C* multi tri-layer upon ion irradiation, using a combination of XSW and *Ni K*-edge XAFS. Our XAFS (and XANES) analysis detects pre-existing charge and atomic transfer at pristine *Ni/C* and *Ni/Pt* interfaces (directly) and determines the character of *Pt/C* to be physically adsorbed *Pt-C* (indirectly). Metallic diffusion into *C* matrix is observed to be directly correlated with the extent of charge transfer at metal /*C* interface. Physical adsorption (at *Pt/C*

interface) evidently encourages interfacial diffusion (*Pt* into *C*). Following irradiation, *Pt* atoms from the disrupted *Pt/C* interfaces migrate towards pre-diffused *Ni* atoms within *C* layer to form *Ni*-centered *Ni-Pt* bimetallic nano-clusters. These clusters having *Ni:Pt* =60:40, are ferromagnetic in nature. The clusters are highly disordered beyond nearest neighbor and resemble the short range order of multi-component glasses. Such disordered clusters on C-matrix have promising applications as magnetic devices.